COMMUNICATION

ADVANCED
INTELLIGENT
SYSTEMS
Open Access

www.advintellsyst.com

Programmable 3D Self-Folding Structures with Strain Engineering

Qiaohang Guo,* Yian Pan, Junjie Lin, Guangchao Wan, Borui Xu, Nengbin Hua, Chan Zheng, Youting Huang, Yongfeng Mei, Wenzhe Chen, and Zi Chen*

Self-assembly of three-dimensional (3D) structures, through bending, twisting, folding, and buckling, has garnered broad interest among physicists, mathematicians, chemists, and biologists. Herein strain engineering and geometric frustration as an on-demand strategy for fabricating spontaneous rolling "origami" structures with programmable multistability across multiple length scales are exploited. Through experiments, theory, and finite element simulations, it is demonstrated that a strain-engineered bilayer structure can make a transition from a monostable, doubly curved shape to a neutrally stable, developable configuration, depending on a dimensionless parameter that is determined through the plate's geometry and misfit strain. In addition, the doubly curved region near the edge can play a significant role in deciding the final bending direction of the strained bilayer due to edge effects. A strain-engineering approach is further proposed to generate various 3D structures by programming the geometry, misfit strain, and mechanical properties of the bilayer units, for instance, a self-folding buckyball structure. These design principles have promising broad applications in constructing self-deploying, stimuli-responsible, and multifunctional devices across multiple length scales.

Morphogenesis, commonly found in leaves,[1–3] flowers,[4,5] cones,[6] seed pods[7,8] and other biological systems, is typically driven by differential growth, swelling, or shrinkage[6,9,10] that occurs within multilayered components of species. For example, the opening and closing of pine cones are attributed to the tissue's self-bending, which undergoes three states of humidity-

driven deformation.[6] As these morphological changes in nature result from the variation of the surrounding environment, it is desirable to mimic these natural examples to fabricate multilayered structures that can spontaneously respond to various external stimuli, such as temperature, pH, biochemical enzymes, magnetic fields, and solvent composition,[11–14] which can find a variety of applications, such as semiconductor nanotubes,[15–18] soft robotics,[19–22] snapping surface,[23] and micro/nanoelectromechanical systems.[24–26]

For a multilayer structure, the misfit strain across layers can lead to some interesting phenomena such as multistability, where more than one stable state exists with the same boundary conditions or control parameters of the system. One specific case is called neutral stability, in which the system can stay stable at each point in a continuous path of shape change. In such a case, the system is said to have zero stiffness because the potential energy of the system keeps unchanged during the shape change and theoretically no external force is needed. Various cases that incorporate neutrally stable (zero stiffness) systems have been studied. Guest et al.[27,28] discovered neutral stability of a heated copper beryllium strip, the shape of which depended on the residual stresses. The strip has zero stiffness for finite deformation along

Prof. Q. Guo, Y. Pan, Prof. N. Hua, Prof. C. Zheng, Prof. Y. Huang
School of Materials Science and Engineering
Fujian University of Technology
Fuzhou 350118, China
E-mail: guoqh@fjut.edu.cn

Prof. Q. Guo
Fujian Provincial Key Laboratory of Advanced Materials Processing
and Application
Fujian University of Technology
Fujian 350118, China

J. Lin, Prof. W. Chen
College of Materials Science and Engineering
Fuzhou University
Fuzhou, Fujian 350108, China

G. Wan, Prof. Z. Chen
Thayer School of Engineering
Dartmouth College
Hanover, NH 03755, USA
E-mail: zi.chen@dartmouth.edu

B. Xu, Prof. Y. Mei
Department of Materials Science State Key Laboratory of ASIC
and Systems
Fudan University
Shanghai 200433, China

Prof. W. Chen
School of Materials Science and Engineering
Xiamen University of Technology
Fujian 361024, China

The ORCID identification number(s) for the author(s) of this article can be found under https://doi.org/10.1002/aisy.202000101.

**ADVANCED
SCIENCE NEWS**
www.advancedsciencenews.com

**ADVANCED
INTELLIGENT
SYSTEMS**
Open Access
www.advintellsyst.com

a twisting path. Holmes et al. exploited the nonhomogenous swelling[29] and isotropic in-plane expansion[30] to drive the dynamical deformation of soft materials that undergo rapid bending and buckling instabilities. In the case of a swelling disc, both the theory and experiments captured the bifurcation and relaxation that occurred when multiple equilibrium states were accessible. Upon bifurcation, a large-amplitude transverse travelling wave rotated azimuthally around the disc with multiple curvatures.[29]

Although neutral stability allows the structure to adopt numerous configurations ideally, many factors, including the geometry, edge effect, and loading history, can affect the final rolling direction.[31–34] For example, Stoychev et al.[33] investigated the folding of rectangular, stimuli-responsive, hydrogel-based, polymer bilayers that can roll along the long side, diagonal, and all sides. They demonstrated that the rolling direction varied depending on different aspect ratios of length to width and relative thickness from experiments and numerical modeling. Although many theoretical and computational works have been performed regarding this topic, the transition between multiple, stable configurations when the bilayer becomes neutrally stable is seldom discussed. Therefore, the general mechanical principle that governs the shape selection of a bilayer with equally biaxial misfit strain needs to be well addressed.

In this study, through a combination of experiments, theory, and finite element simulations, we study the mechanism of the complex rolling behavior and programmability of these neutral stable 3D morphologies generated from flat 2D bilayer precursors. By utilizing the obtained results, we present a strain-engineered approach for creating versatile 3D self-folding structures. The rest of the article is organized as follows. First, we demonstrate the existence of neutral stability with a bilayer rubber strip with equally biaxial misfit strain between layers and investigate the effect of the bilayer's geometry on the actual rolling direction. Then a theoretical framework is proposed to address the transition from monostability to neutral stability, which is controlled by a dimensionless parameter. In addition, the effect from the doubly curved, narrow region near the edge on the actual bending direction of the bilayer is discussed. Furthermore, we show that many different shapes can be generated using this strain-engineering approach. Finally, we design and fabricate a complex self-folded device that resembles a buckyball. This mechanism, when combined with other actuation methods, can be used to create shape-programmable smart structures or devices with multiple stable configurations for a wide range of applications.

In our experiments, one sheet of latex rubber (Young's modulus $E_1 = 1.65$ MPa, thickness $H_1 = 0.25$ mm, Poisson's ratio $\nu_1 = 0.49$) is prestretched in the mutually perpendicular directions $\overrightarrow{r_1}$ and $\overrightarrow{r_2}$ with the same strain values ($\varepsilon_1 = \varepsilon_1 = 0.18$) and bonded to an elastic strip ($E_2 = 10.5$ MPa, $H_2 = 1.00$ mm, $\nu_2 = 0.35$), whose top is coated with a thin red layer of latex rubber to prevent it from getting dirty. The longitudinal direction of the composite strip $\overrightarrow{d_x}$ forms a misorientation angle ϕ with the direction $\overrightarrow{r_1}$. When cut from the sheet along the dotted line as shown in **Figure 1**a, the bilayer will roll up driven by the residual stress. By changing the bilayer's geometry, including the length L, the width W, and the total thickness H (Figure 1b), we can change the rolling direction of the bilayer with the mechanical properties fixed.

When the bilayer is slim and long ($W = 5$ mm, $L = 95$ mm, $\phi = 0°$), it adopts a ring-like configuration (Figure 1c) by rolling along the longitudinal direction $\overrightarrow{d_x}$. To test the effect of the misorientation angle ϕ on the rolling direction, 12 strips are arranged in a pattern in which each strip is separated by the adjacent ones by a $\pi/6$ interval (Figure 1d) and these strips are bonded to a prestretched bottom layer. Once released, the star-shaped bilayer bends to form a Tire shape (Figure 1e), which means the bending direction is independent of the misorientation angle.

When the bilayer is large and long enough ($W = 48$ mm, $L = 350$ mm), it adopts a cylindrical configuration with a constant radius almost everywhere except near the edges (**Figure 2**a). Interestingly, the bilayer can be easily and continuously twisted either clockwise or anticlockwise to a new, stable configuration with no stiffness when subjected to a small driving force. Therefore, the shell is held in place by no more than the friction provided by the underlying surface and indicates the existence of neutral stability (also see Movie S1, Supporting Information). Balancing friction or surface adhesion with elasticity will enrich the design space and introduce new multistable configurations, yet here we opt to focus on the use of neutral stability that mainly arises from elasticity. We also develop and present a full 3D COMSOL5.5 finite element model to conduct simulations using the structural mechanics module. The mechanical properties of the materials are assumed to be isotropic and linear elastic. For simplicity, here we make some simplifications in bilayer structures, such as ignoring the effect of the thin red layer of the latex rubber on the top. The parameters in the bilayer used are the same as in the experiments, including the prestrain ($\varepsilon_1 = \varepsilon_1 = 0.18$), the sizes of geometry ($W = 48$ mm, $L = 350$ mm, $H_1 = 0.25$ mm, $H_2 = 1.00$ mm), Poisson's ratio ($\nu_1 = 0.49$, $\nu_2 = 0.35$), Young's modulus ($E_1 = 1.65$ MPa,
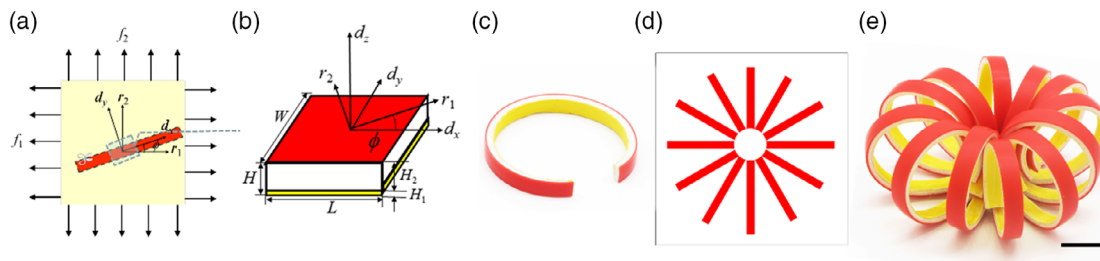

Figure 1. a) Schematic illustration of the fabrication of the bilayer strip with residual stress. b) The geometry of the bilayer strip. c) A ring-like configuration. d) Schematic illustration of a star-shaped bilayer precursor. e) A tire-shaped configuration after release. Scale bar = 10 mm.

ADVANCED
SCIENCE NEWS
www.advancedsciencenews.com

ADVANCED
INTELLIGENT
SYSTEMS
Open Access
www.advintellsyst.com

Figure 2. a) A series of different configurations of the neutrally stable structure with the same radius of 42 mm, which can be transformed between configurations in each direction in experiments. b) FEM solid model built in COMSOL5.5 for the estimation of the stress and distortion profile. Bar = 50 mm.

$E_2 = 10.5$ MPa), other material parameters, and the mis-orientation angle between the principal axes of the prestretch and the geometric axes ϕ. In this model, the mutually perpendicular strain tensor of the prestretch in the bottom layer is

$$\boldsymbol{\varepsilon} = (\varepsilon_1 \cos^2 \phi + \varepsilon_2 \sin^2 \phi)\mathbf{e}_1 \otimes \mathbf{e}_1 + (\varepsilon_1 \sin^2 \phi + \varepsilon_2 \cos^2 \phi)\mathbf{e}_2 \otimes \mathbf{e}_2 + (\varepsilon_1 - \varepsilon_2) \sin \phi \cos \phi (\mathbf{e}_1 \otimes \mathbf{e}_2 + \mathbf{e}_2 \otimes \mathbf{e}_1) \tag{1}$$

Assuming $\varepsilon_0 = \varepsilon_1 = \varepsilon_2$, we can get $\boldsymbol{\varepsilon} = \varepsilon_0(\mathbf{e}_1 \otimes \mathbf{e}_1 + \mathbf{e}_2 \otimes \mathbf{e}_2)$. Thus, whatever the value of ϕ takes, it will not affect the strain tensor. In the finite element simulations that follow the same procedures in our previous works,[35–37] we adopt the method of perturbation (1% of the prestress) and push directly at both ends of the diagonal of the bottom layer to model the shape transition. The bilayer is coiled about an axis inclined to the bilayer length after applying small forces in different directions between its ends (Figure 2b). Although there are some deviations between the simulation results and the experiments, especially the circular configuration in the middle of Figure 2b as shown, most simulation results are consistent with the experiments.

The experimental results indicate the existence of neutral stability. Next, we use a theoretical framework to interpret the experimental observation. We consider a composite bilayer of width W, length L, and total thickness H ($H \ll W \ll L$) consisting of two sheets of different materials that are bonded together. The bilayer is initially flat. Then the surface stress is applied on one layer. As a result, the bilayer structure will morph into a 3D configuration with the principal curvatures κ_1 and κ_2 along the principal directions of the surface stresses (Figure 1b). Based on the linear elasticity theory, the total potential energy per unit length of the bilayer is contributed from the surface stresses (Π_s), bending energy (Π_b), and stretching energy due to geometric nonlinearity (Π_g) as[38,39]

$$\Pi = \Pi_s + \Pi_b + \Pi_g \tag{2}$$

where

$$\Pi_s = -WH(f_1 \kappa_1 + f_2 \kappa_2)/2 \tag{3}$$

$$\Pi_b = EH^3 W(\kappa_1^2 + \kappa_2^2 + 2\nu\kappa_1\kappa_2)/24(1-\nu^2) + O(EH^3 W^3 \kappa^4) \tag{4}$$

$$\Pi_g = EHW^5(\kappa_1\kappa_2)^2/[640(1-\nu^2)] + O(EHW^7\kappa^6) \tag{5}$$

$O(EH^3 W^3 \kappa^4, EHW^7 \kappa^6)$ are the higher order terms of the bending and stretching energy. f_1 and f_2 are the principal surface stresses. The parameters E and ν are the effective Young's modulus and Poisson's ratio of the composite bilayer, respectively.

Here, we extend this theory to illustrate the underlying mechanism of the morphological transition and multistability of the bilayer in our case. On one hand, the mismatch strain between the top and bottom layers due to the prestretching can be equivalently taken as the surface stress acting on one layer. On the other hand, when the bending and stretching energy are of comparable magnitude, geometrical incompatibility may cause bifurcation.[7,39,40] Comparing the scale of Π_b and Π_g, we can get a characteristic width, $W_0 \approx 2.28\sqrt{H/\kappa}$ ($\kappa = \max\{\kappa_1, \kappa_2\}$, $\nu = 0.49$). Such a length scale can be used to define the doubly curved, narrow region close to the edge, which has been analyzed by Holmes,[30] Sharon,[7,8] and our previous study.[38,39] To obtain the equilibrium shapes of the bilayer, we apply the stationary condition ($\partial\Pi/\partial\kappa_i = 0$, $i = 1, 2$). As the misfit strain across layers is equally biaxial, we set the effective surface stress as $f = f_1 = f_2$ and have the governing equation regarding the equilibrium shapes as $(\kappa_1 - \kappa_2)[\kappa_1\kappa_2 - 80(1+\nu)H^2/(3W^4)] = 0$.

The governing equation, which is expressed in terms of the principal curvatures κ_1 and κ_2, can be satisfied by letting either $\kappa_1 - \kappa_2$ or $\kappa_1\kappa_2 - 80(1+\nu)H^2/3W^4$ equal to zero. If the final shape is determined through $\kappa_1 = \kappa_2$, the bilayer will deform into a spherical shallow cap. Otherwise, if $\kappa_1\kappa_2 - 80(1+\nu)H^2/(3W^4) = 0$ has two real solutions, the bilayer will undergo cylindrical bending and become neutrally stable because the principal direction can be arbitrary when the surface stress is equally biaxial. Therefore, bifurcation happens when both $\kappa_1 = \kappa_2 = \kappa$ and $\kappa_1\kappa_2 = 80(1+\nu)H^2/(3W^4)$ are satisfied. In such a scenario, both principal curvatures (κ_1, κ_2) are equal to $6.3H/W^2$ for $\nu = 0.49$. Defining the dimensionless parameter $\eta \equiv W\sqrt{\kappa/H}$ and substituting κ, we can get the critical dimensionless parameter $\eta_c \approx 2.51$, which is also equal to the case when two layers of latex rubber are prestretched along perpendicular directions by an equal amount and bonded together.[7,8,39] Using the aforementioned theoretical analysis, the bifurcation width in our experiment can be calculated as $W_C \approx 2.51\sqrt{\frac{H}{\kappa}} = 24.7$ mm.

The ratio of the stretching energy and bending energy scales as $\Pi_g/\Pi_b \sim W^4\kappa^2/H^2 = \eta^4$. When $\eta \ll \eta_c$, the equilibrium configuration is dominated by the bending energy, and the stretching energy associated with the nonzero Gaussian curvature can be ignored. Notably, the helix angle Φ is determined by the following equation[41,42]

$$\Phi = \arctan\left[(\kappa_1 - \kappa_2)\sin\phi\cos\phi/\sqrt{\kappa_1^2\cos^2\phi + \kappa_2^2\sin^2\phi}\right] \tag{6}$$

ADVANCED
SCIENCE NEWS

www.advancedsciencenews.com

ADVANCED
INTELLIGENT
SYSTEMS
Open Access

www.advintellsyst.com

As $\kappa_1 = \kappa_2$, the misorientation angle ϕ, regardless of the curvature and the value of the helix angle, is always equal to zero. Thus, when $\eta \ll \eta_c$, the bilayer will become either a ring-like shape when it has narrow width and long length or a spherical shallow cap if the width is relatively the same as the length. This analysis is consistent with the aforementioned experiments, as shown in Figure 1c.

When $\eta \gg \eta_c$, the stretching energy Π_g dominates. To minimize the total energy, the geometric nonlinearity requires that either $\kappa_1 \to 0$ or $\kappa_2 \to 0$, which means that the Gaussian Curvature $K = \kappa_1 \kappa_2$ goes to zero for the majority of the bilayer (except near the edges) to reduce the stretching energy. Otherwise, the stretching energy will become very large compared to the bending energy, which is inadmissible. Zero Gaussian curvature of a surface is known to correspond to a flat or a cylindrical configuration. In this case, the bilayer prefers a cylindrical configuration rather than being flat to reduce the bending energy. Without losing generality, we assume $\kappa_2 = 0$. Here, the potential energy density can be obtained by considering the misorientation ϕ

$$\Pi_2^*(\phi) = -3(1 - \nu^2)(f_1 \cos^2 \phi + f_2 \sin^2 \phi)^2/(2EH) \qquad (7)$$

For different misorientation angles, the potential energy density keeps invariant for $f_1 \cos^2 \phi + f_2 \sin^2 \phi = f$. Thus, Π_2^* remains a constant regardless of the misorientation angle ϕ. By minimizing the energy density, we obtained the principal curvature $\kappa_1 = 6f(1 - \nu^2)/(EH^2)$. In such a case, the bilayer possesses neutral stability with zero twisting rigidity (Figure 2), indicating that it can be twisted arbitrarily to a new stable shape with the same curvature in any direction without changing its potential energy, if edge effect is not considered.

As observed in the experiments, it is worth mentioning that the edge effects can change the energy distribution of the bilayer structure. Therefore, the nonzero Gaussian curvature near the edge needs to be taken into account in most cases. The potential energy density is no longer Π_2^* for the bilayer. By calculating the energy density within a narrow region from the edge, we noted that $\Pi_b \gg \Pi_g$, the bending energy dominates. The density of the potential energy is Π_1^*. As $\Pi_2^*(\phi) = -3(1 - \nu^2)f^2/(2EH) > \Pi_1^* = -6(1 - \nu)f^2/(EH)$, it clearly shows that the edge effect

reduces the total potential energy. If the width of the boundary region keeps unchanged, enlarging the boundary's length is the most effective way to reduce the total potential energy. Thus, the bilayer will roll along the longitudinal direction to enlarge the area of the doubly curved boundary region.

When $\eta \gg \eta_c$, the bilayer contains neutral stability if we do not consider the edge effect. If we take the edge effect into account, the bilayer prefers a coiled configuration instead of a helix or cigar, provided that the 2D precursor is a long and large rectangle ($L \gg W \gg W_c$). As a result, the coiled shape becomes the most stable compared to other stable configurations because it contains the lowest potential energy. For a square precursor, the bilayer can stay stable along many directions (**Figure 3**a–d). It seems that there is not a preferred bending direction, probably because the potential energy's reduction brought about by the edge effect is almost the same for any bending direction. However, if we increase the mismatch strain from 0.18 to 0.20, the bilayer prefers to bend along the diagonal direction—if we force the bilayer to bend along the other direction, it can only stay stable for a while and then becomes unstable by automatically switching to the diagonal direction. (Movie S2, Supporting Information).

By decreasing the prestretch strain or the geometric dimensions of the 2D precursor, η will decrease and become equal to or lower than η_c. Accordingly, the bilayer will curve along the diagonal directions ($W = 18$ mm, $L = 36$ mm; Figure 3e) or form a shallow spherical cap with equal curvatures (Figure 3f), respectively. When $\eta \sim \eta_c$, the energy of bending and stretching are of the same magnitude in this situation, and the bilayer shows monostability rather than neutral stability. To minimize the total potential energy, as discussed previously, the bilayer will still roll along the longitudinal direction, similar to the result of Alben et al.[32] Here, we also try to decrease the pre-stretch of the square bilayer to 0.05 ($W = L = 48$ mm), the bilayer shows monostability by adopting the shape of a spherical shallow cap (Figure 3g). In this situation, furthermore, by decreasing the strain of the prestretch to 0.1 and increasing the thickness of H_2 to 2.00 mm (Figure 3h), the bilayer will show a similar morphology to that in Figure 3g.

More generally, our theory and simulation can not only work for the bilayer with a rectangular planform, but also work for
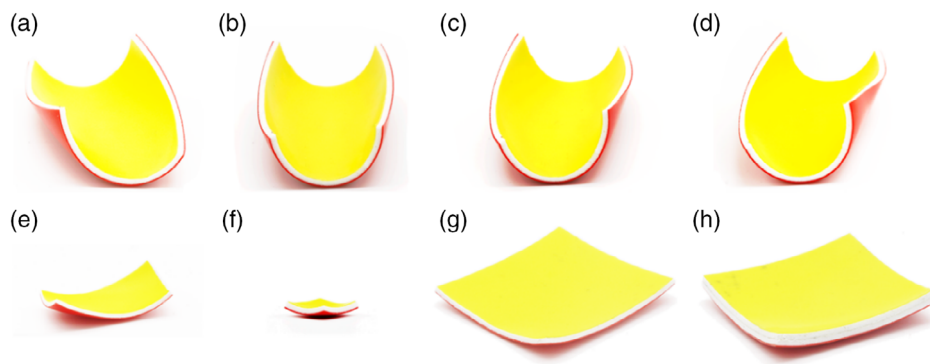

Figure 3. The shapes of the bilayers under different geometries and misfit strains. a–d) neutrally stable along four different bending directions ($W = L = 48$ mm, $H_2 = 1.00$ mm, $p = q = 0.18$). e) Monostable configuration with diagonal rolling direction ($W = 18$ mm, $L = 36$ mm, $p = q = 0.18$). f–h) Monostable configuration with the shape of a spherical shallow cap, f) $W = L = 16$ mm, $H_2 = 1.00$ mm, $p = q = 0.18$; g) $W = L = 48$ mm, $H_2 = 1.00$ mm, $p = q = 0.05$; and h) $W = L = 48$ mm, $H_2 = 2.00$ mm, $p = q = 0.1$. Scale bar = 10 mm.

ADVANCED
SCIENCE NEWS
www.advancedsciencenews.com

ADVANCED
INTELLIGENT
SYSTEMS
Open Access
www.advintellsyst.com

many other planforms' shapes, such as triangle (**Figure 4**a,d,g), pentagon (Figure 4b,e,h), and hexagon (Figure 4c,f,j). In our simulations, the stress and distortion of the pattern are obtained from different geometric parameters with the same pre-strain, which is consistent with our experiments (Figure S1, Supporting Information). In these experiments, the width and length in a rectangular case is replaced by a short axis and long axis, respectively. If the 2D precursor is circular with rotational symmetry, the configuration will show a spherical cap ($\eta \ll \eta_c$) or neutrally stable cylindrical shape ($\eta \gg \eta_c$) without a preferred bending direction.

The proposed theoretical framework is scalable and independent of the constituent materials. To demonstrate this, we perform experiments in the ultrathin system with different materials rather than a rubber sheet. Here, polydimethylsiloxane (PDMS, Dow Corning's Sylgard 184) is synthesized by mixing the base/curing agent in a 10:1 ratio by weight. After being stirred, the mixture is put into a vacuum chamber to remove the air bubbles and then spin coated on a clean glass substrate.

After the PDMS is cured at 80 °C for 3 h, an aluminum (Al) film is deposited by a direct current (DC) magnetron sputtering technique with a temperature of 100 °C for heating on the PDMS layer. During film deposition, the argon pressure and sputtering power are kept at 0.4 Pa and 30 W, respectively. The thickness of the PDMS layer and Al film is 400 and 360 nm, respectively. The elastic modulus of PDMS, measured by uniaxial tensile testing (UTM2102 SHIMADZU Company), is 1.6 MPa and that of Al film, tested by atomic force microscope (Bruker Icon), is 45 GPa. The Poisson's ratio of PDMS and Al roughly equals 0.49 and 0.35, respectively. During the sputtering, thermal stress is generated, which leads to the following 3D large deformation. Here, we detach the PDMS–Al bilayer from the glass with various 2D geometries and the released bilayer will curl to an arc (**Figure 5**f) or show neutrally stable configurations (Figure 5a–e), among which the bilayer structure with zero stiffness can be transformed. Similarly, neutral stability is achieved when the bilayer's width is beyond the critical width ($W_C = 2.51\sqrt{H/\kappa} \approx 5.0$ mm).
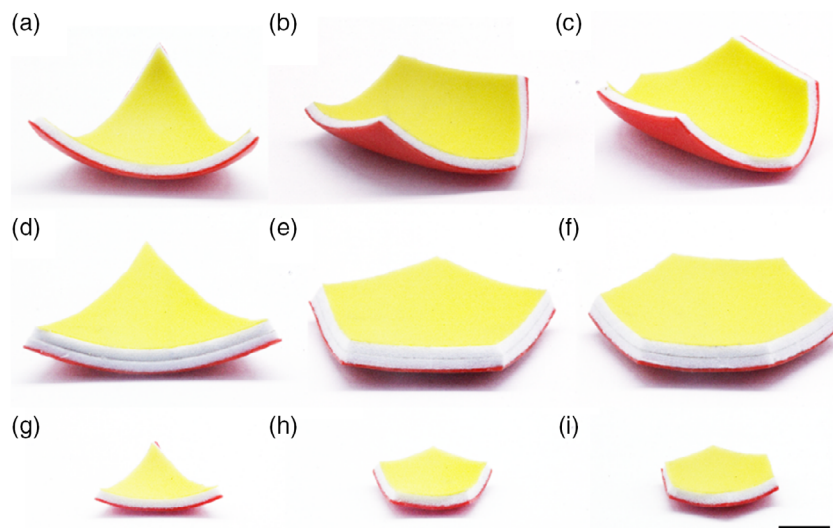

Figure 4. The configurations of the regular pentagon with equal prestrain ($p = q = 0.18$): a–c) neutrally stable state (the circumcircle radius of the polygons (R) is 20 mm, $H_2 = 1.00$ mm); d–f) monostable state ($R = 20$ mm, $H_2 = 2.00$ mm); g–i) monostable state ($R = 10$ mm, $H_2 = 1.00$ mm). Scale bar = 10 mm.
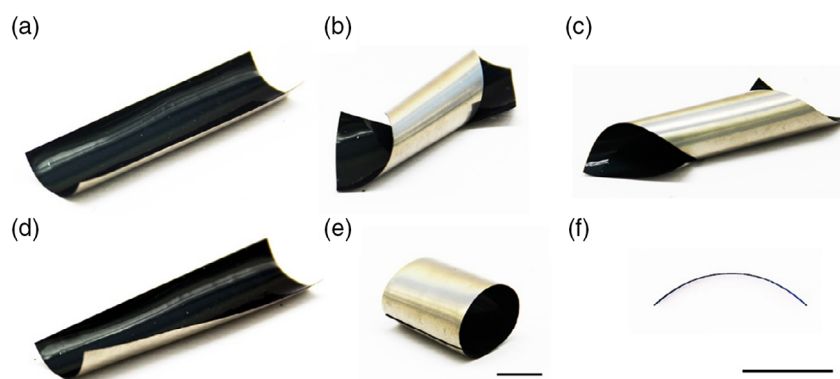

Figure 5. Different configurations of the PDMS–Al bilayer. a–e) The neutrally stable structure ($W = 19.5$ mm, $L = 54.5$ mm); f) a segment of the ring-like configuration ($W = 1.0$ mm, $L = 1.95$ mm). Scale bar = 10 mm.

In addition to the PDMS–Al bilayer, we also choose another nanoscale metallic system to demonstrate the generality of our results. Here, e-beam evaporation was applied to deposit a film consisting of Ag, SiO$_2$, and Cr on glass substrate.[43] The thickness of each layer was tuned as 40 nm, which means that the total thickness is 120 nm. A residual stress gradient along the z axis was established during the deposition as a consequence of thermal expansion mismatch. Then, a drop of ethanol was used to peel off the film from the substrate and the rolling direction was determined by the contact point between the liquid and ultrathin film. A variety of configurations were obtained in **Figure 6**a–e. Considering that the total thickness is about hundreds of nanometers while the rolling diameter was measured as ≈20 μm, the width of the film is much larger than the critical width, leading to a neutrally stable state with multiple possible configurations. Such self-rolling structures have been demonstrated to have applications in vapor sensing,

microresonators, micromotors, and microactuators.[43] Another potential application is to use these neutral stable structures in energy harvesting[44–46] by using piezoelectric materials in them, as these structures have minimum twisting stiffness and will manifest deformation and therefore energy-harvesting efficiency from the environment. It is also anticipated that by incorporating these smart structural elements, a variety of novel structures and devices, including mechanical metamaterials[47] and flexible robotics,[48,49] can be obtained.

We have shown that one bilayer precursor can morph into various rolling configurations if it is neutrally stable. By assembling several or more bilayer precursors together, we are able to generate a variety of 3D structures by programming the geometry and misfit strain in each layer. The dimensionless parameter η, here, is crucial to determining the multistability of the bilayer, which is associated with not only the width and thickness, but also the misfit strain. In addition, the curvature of the deformed
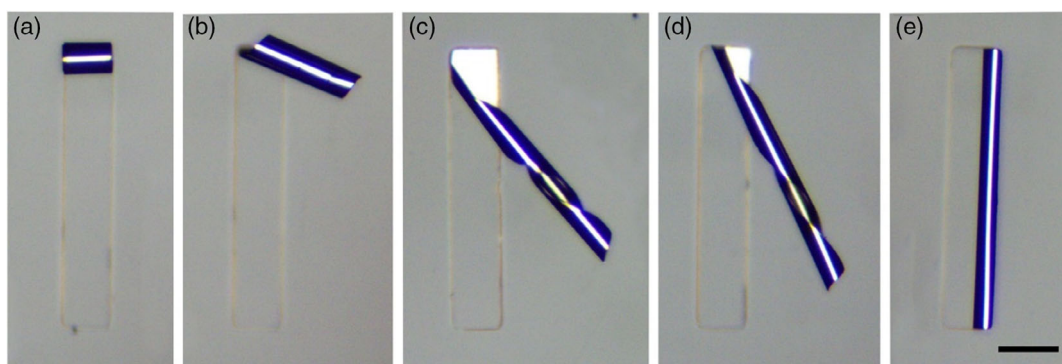

Figure 6. Different configurations of an ultrathin film ($H = 120$ nm) consisting of Ag, SiO, and Cr. a–e) The neutrally stable structure ($W = 50$ μm, $L = 400$ μm). Scale bar = 100 μm.
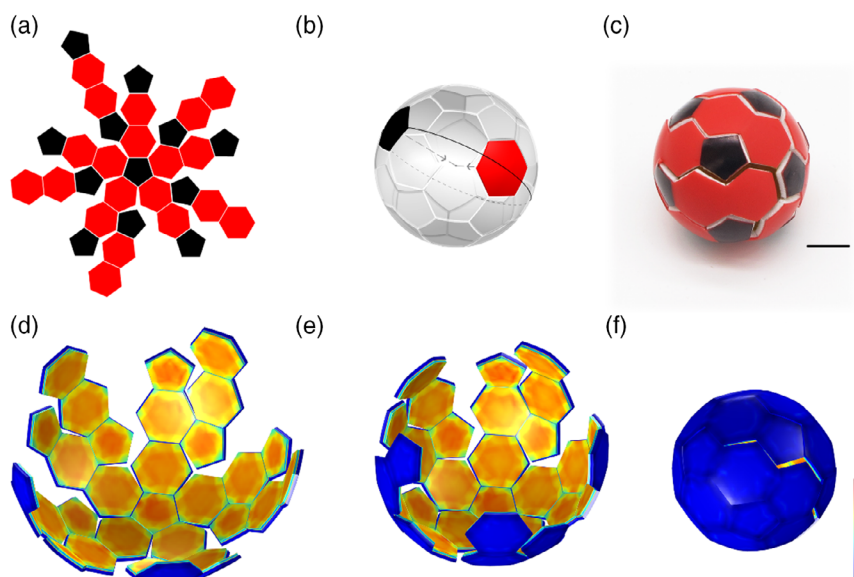

Figure 7. a) Schematic illustration of polygons' pattern for the top layer. b) The relationship of the radius between the polygons and the spherical shell at the maximum cross-section. c) The graph of a buckyball self-folded conformation. d–f) The stress pattern (blue means low and red means high) and distortion of the bilayer by finite element simulation (the value of the mismatched strain is 0.093, 0.120, and 0.180, respectively). Bar = 10 mm.

structure is also a function of surface stress, elastic modulus, and thickness. Therefore, either reducing width (Figure 3f), misfit strain (Figure 3g), or increasing thickness (Figure 3h) can transition the bilayer from neutral stability to monostability.

Based on our aforementioned mechanical model, many complex shapes can be designed for a variety of engineering applications. Here, we propose a self-folding design scheme to produce a buckyball structure. To accomplish this aim, the bottom layer is prestretched, as mentioned previously. The top layer, which is shown in **Figure 7**a, consists of 12 pentagons and 20 hexagons. The essence of this design is that the radius of the ball should equal to the radius of the polygon's curvature (Figure 7b). As Figure 1c shows, the curvature of the bilayer with narrow width is $\approx 0.048\,mm^{-1}$, while the equally biaxial misfit strain is 0.18. The circumference of the maximum cross-section of a football, which equals approximately the sum of four times the height of the pentagon, four times the height of the hexagon, and two times the length of the hexagon, should be 131 mm in this case. To decrease the interaction between polygons and prevent the bilayer from transforming from monostability to neutral stability, each interval of the polygon connection is set as 1 mm. Thus, the polygon side length approaches 8 mm based on the aforementioned analysis. According to the design, the self-folding bilayer of a buckyball structure can be generated and shown in Figure 7c. In the finite element method (FEM) modeling, the stress distribution within the elastic bilayer that undergoes large distortion is shown in Figure 7d–f.

In summary, we developed an on-demand strategy for fabricating neutrally stable structures in a variety of strain-engineered systems across multiple length scales and used a theoretical model to address the transition between mono- and neutral stability driven by an equally biaxial mismatch strain. A dimensionless parameter is used to describe the bifurcation and the edge effect can determine the final status of the bilayer. The model can predict the transition between monostability and neutral stability in most arbitrary geometric shapes in various materials. Moreover, we offer a simple approach using strain engineering to achieve self-folding structures and therefore this study can expect to find ample applications in the design of microscale capsule casing, energy harvesting, microrobotics, mechanical metamaterials, stimuli-responsive reconfigurable structures,[50–52] and other multifunctional devices.

Supporting Information

Supporting Information is available from the Wiley Online Library or from the author.

Conflict of Interest

The authors declare no conflict of interest.

[1] A. S. Westermeier, R. Sachse, S. Poppinga, P. Vögele, L. Adamec, T. Speck, M. Bischoff, *P. R. Soc. B-Biol. Sci.* **2018**, *285*, 20180012.
[2] Q. Guo, E. Dai, X. Han, S. Xie, E. Chao, Z. Chen, *J. R. Soc. Interface* **2015**, *12*, 598.
[3] M. Han, S. Ahn, *Adv. Mater.* **2017**, *29*, 1606580.
[4] H. Liang, L. Mahadevan, *Proc. Natl. Acad. Sci.* **2011**, *108*, 5516.
[5] J. Li, M. Liu, W. Xu, H. Liang, L. Liu, *Comput. Anim. Virtual W.* **2015**, *26*, 433.
[6] S. Lin, Y. M. Xie, Q. Li, X. Huang, S. Zhou, *Soft Matter* **2016**, *12*, 9797.
[7] S. Armon, E. Efrati, R. Kupferman, E. Sharon, *Science* **2011**, *333*, 1726.
[8] H. Aharoni, S. Armon, E. Sharon, *Soft Matter* **2014**, *16*, 2733.
[9] J. Wang, G. Wang, X. Feng, T. Kitamura, Y. Kang, S. Yu, S. Qin, *Sci. Rep.* **2013**, *3*, 3101.
[10] R. Kennaway, E. Coen, A. Green, A. Bangham, *Plos. Comput. Biol.* **2011**, *7*, 1002071.
[11] Y. S. Zhang, K. Yue, J. Aleman, K. Mollazadeh-Moghaddam, S. M. Bakht, J. Yang, W. Jia, V. E. Dell, P. Assawes, S. R. Shin, *Ann. Biomed. Eng.* **2017**, *45*, 148.
[12] X. Li, M. J. Serpe, *Adv. Funct. Mater.* **2014**, *24*, 4119.
[13] A. M. Abdullah, P. V. Braun, K. J. Hsia, *Soft Matter* **2016**, *12*, 6184.
[14] J. C. Athas, C. P. Nguyen, B. C. Zarket, A. Gargava, Z. Nie, S. R. Raghavan, *ACS Appl. Mater. Interface.* **2016**, *8*, 19066.
[15] B. Xu, B. Zhang, L. Wang, G. Huang, Y. Mei, *Adv. Funct. Mater.* **2018**, *28*, 1705872.
[16] L. Dai, L. Zhang, *Nanoscale* **2013**, *5*, 971.
[17] Z. Tian, W. Huang, B. Xu, X. Li, Y. F. Mei, *Nano Lett.* **2018**, *18*, 3688.
[18] N. Hu, R. Burgueño, *J. Appl. Mech.* **2017**, *84*, 11003.
[19] D. Rus, M. T. Tolley, *Nature* **2015**, *521*, 467.
[20] H. Zeng, P. Wasylczyk, D. S. Wiersma, A. Priimagi, *Adv. Mater.* **2017**, *30*, 1703554.
[21] M. Pilz Da Cunha, S. Ambergen, M. G. Debije, E. F. G. A. Homburg, J. M. J. den Toonder, A. P. H. J. Schenning, *Adv. Sci.* **2020**, *7*, 1902842.
[22] H. Huang, M. S. Sakar, A. J. Petruska, S. Pané, B. J. Nelson, *Nat. Commun.* **2016**, *7*, 12263.
[23] M. Pezzulla, N. Stoop, M. P. Steranka, A. J. Bade, D. P. Holmes, *Phys. Rev. Lett.* **2018**, *120*, 048002.
[24] W. Huang, Z. Yang, M. D. Kraman, Q. Wang, Z. Ou, M. M. Rojo, A. S. Yalamarthy, V. Chen, F. Lian, J. H. Ni, S. Liu, H. Yu, L. Sang, J. Michaels, D. J. Sievers, J. G. Eden, P. V. Braun, Q. Chen, S. Gong, D. G. Senesky, E. Pop, X. Li, *Sci. Adv.* **2020**, *6*, 4508.
[25] T. Y. Huang, H. W. Huang, D. D. Jin, Q. Y. Chen, J. Y. Huang, L. Zhang, H. L. Duan, *Sci. Adv.* **2020**, *6*, 8219.
[26] H. Ko, L. F. Deravi, S. J. Park, J. Jang, T. Lee, C. Kang, S. L. Jin, K. K. Parker, K. Shin, *Adv. Mater.* **2017**, *29*, 1701732.

[27] S. Guest, E. Kebadze, S. Pellegrino, *J. Mech. Mater. Struct.* **2011**, *6*, 203.

[28] K. A. Seffen, S. D. Guest, *J. Appl. Mech.* **2011**, *78*, 141.

[29] D. P. Holmes, M. Roché, T. Sinha, H. A. Stone, *Soft Matter* **2011**, *7*, 5188.

[30] M. Pezzulla, G. Smith, P. Nardinocchi, D. P. Holmes, *Soft Matter* **2016**, *12*, 4435.

[31] I. S. Chun, A. Challa, B. Derickson, K. J. Hsia, X. Li, *Nano Lett.* **2010**, *10*, 3927.

[32] S. Alben, B. Balakrisnan, E. Smela, *Nano Lett.* **2011**, *11*, 2280.

[33] G. Stoychev, S. Zakharchenko, S. Turcaud, J. W. C. Dunlop, L. Ionov, *ACS Nano* **2012**, *6*, 3925.

[34] G. Stoychev, A. Kirillova, L. Ionov, *Adv. Opt. Mater.* **2019**, *7*, 1900067.

[35] Z. Chen, *Nanoscale* **2014**, *6*, 9443.

[36] Q. Guo, H. Zheng, W. Chen, Z. Chen, *Bio-med. Mater. Eng.* **2014**, *24*, 557.

[37] Z. Chen, *Arch. Appl. Mech.* **2015**, *85*, 331.

[38] Q. Guo, A. K. Mehta, M. A. Grover, W. Chen, D. G. Lynn, Z. Chen, *Appl. Phys. Lett.* **2014**, *104*, 211901.

[39] Z. Chen, Q. Guo, C. Majidi, W. Chen, D. J. Srolovitz, M. P. Haataja, *Phys. Rev. Lett.* **2012**, *109*, 114301.

[40] L. B. Freund, *J. Mech. Phys. Solids.* **2000**, *48*, 1159.

[41] Z. Chen, C. Majidi, D. J. Srolovitz, M. Haataja, *Appl. Phys. Lett.* **2011**, *98*, 011906.

[42] Q. Guo, Z. Chen, W. Li, P. Dai, K. Ren, J. Lin, A. L. Taber, W. Chen, *Europhys. Lett.* **2014**, *105*, 64005.

[43] B. Xu, X. Zhang, Z. Tian, D. Han, X. Fan, Y. Chen, Z. Di, T. Qiu, Y. Mei, *Nat. Commun.* **2019**, *10*, 5019.

[44] L. Dong, A. B. Closson, C. Jin, Y. Nie, A. Cabe, D. Escobedo, S. Huang, I. Trase, Z. Xu, Z. Chen, M. D. Feldman, J. X. J. Zhang, *Adv. Healthcare Mater.* **2020**, *9*, 2000053.

[45] L. Dong, C. Jin, A. B. Closson, I. Trase, H. R. Richards, Z. Chen, J. X. J. Zhang, *Nano Energy* **2020**, *76*, 105076.

[46] L. Dong, A. B. Closson, M. Oglesby, D. Escobedo, C. Jin, X. Han, Y. Nie, S. Huang, Z. Xu, M. D. Feldman, Z. Chen, J. X. J. Zhang, *Nano Energy* **2019**, *66*, 104085.

[47] D. Z. Rocklin, S. Zhou, K. Sun, X. Mao, *Nat. Commun.* **2017**, *8*, 14201.

[48] C. Jin, J. Zhang, I. Trase, S. Huang, Z. Xu, L. Dong, Z. Liu, S. Usherwood, J. X. J. Zhang, Z. Chen. *Adv. Intell. Syst.* **2020**, 1900162.

[49] B. Xu, X. Han, Y. Hu, Y. Luo, C.-H. Chen, Z. Chen, P. Shi, *Small* **2019**, *15*, 1900006.

[50] M. Li, Z. Jiang, N. An, J. Zhou, *Int. J. Mech. Sci.* **2018**, *140*, 271.

[51] N. An, M. Li, J. Zhou, *Smart Mater. Struct.* **2016**, *25*, 11LT02.

[52] W. Guo, M. Li, J. Zhou, *Smart Mater. Struct.* **2013**, *22*, 115028.